Device-Level Simulation of Wave Propagation Along Metal–Insulator–Semiconductor Interconnects

Gaofeng Wang, *Senior Member, IEEE*, Robert W. Dutton, *Fellow, IEEE*, and Conor S. Rafferty, *Fellow, IEEE*

***Abstract*—A device-level simulation is presented for studying wave propagation along metal–insulator–semiconductor interconnects. A set of nonlinear equations is first formulated by combining the motion equations of charged carriers and Maxwell's equations. The set of nonlinear equations is then transformed into the frequency domain, which leads to sets of nonlinear equations for the fundamental mode and its harmonics. Finally, the sets of nonlinear equations in the frequency domain are discretized using the finite-element method and solved using Newton's iterations. Special numerical enhancements are implemented to speed up the computational convergence and handle the boundary layer nature of the problem under study. This device-level simulation provides knowledge on field–carrier interactions, semiconductor substrate loss, and nonlinearity, as well as slow-wave and screening effects of charged carriers. This device-level simulation scheme enables a rigorous full-wave study of nonlinearity effects that arise from semiconductor substrates. Numerical examples for some practical material and geometrical parameters are included to illustrate capabilities and efficiency of the proposed device-level simulation scheme.**

***Index Terms*—Boundary layer problem, device-level simulation, electromagnetic analysis, field–carrier interactions, finite-element method, MIS interconnects, semiconductor nonlinearity and loss, slow-wave effect.**

I. Introduction

EFFECTS of on-chip interconnects are becoming a limiting factor to the overall performance of circuits due to denser and larger chips and higher clock rates. Today, the on-chip wiring delays become much more significant portions of the total chip delays than in the past. Interconnect effects such as losses, dispersion, and substrate noise may degrade the performance of circuits. Metal–insulator–semiconductor (MIS) interconnects, being one of the most elementary components in the modern integrated circuits, have been of fundamental interest. Slow-wave propagation in MIS and Schottky-contact interconnects has been both experimentally observed and theoretically explained from different points-of-view [1]–[5]. The slow-wave properties of such interconnects can be employed to reduce the size and cost of distributed elements to implement delay lines, variable phase shifters, voltage-tunable filters, etc. On the other hand, the energy dissipation in both the semiconductor layer and conductor line may have significant impact on the performance of MIS interconnects. Moreover, the nonlinear nature of semiconductor substrates of on-chip interconnects has been systematically ignored by most previous research. The question when the nonlinearity of on-chip interconnects can be safely neglected is, however, not answered adequately and quantitatively. In order to understand mechanisms behind various effects such as substrate noise, semiconductor nonlinearity and loss, conductor loss, slow-wave effect, or dispersion it is necessary to accurately simulate the MIS interconnect structures.

Analytical or empirical lumped-circuit models [6], [7] were used to provide fast calculation and firsthand insight to the performance of MIS interconnects. However, they are applicable to a few simplified configurations only and provide very limited information about the distributed nature of MIS interconnects. Nevertheless, the lumped-circuit models can be employed to initialize more powerful numerical algorithms.

More accurate analysis of MIS interconnects requires the solution of the electromagnetic-field problem. Numerical schemes for electromagnetic simulation of MIS interconnects include the mode-matching method [8], [9], the spectral-domain analysis (SDA) method [10]–[12], the method of lines [13], the transmission-line matrix (TLM) method [14], the finite-difference time-domain (FDTD) method [15], and the finite-element method [16], [17]. In these purely electromagnetic simulation models, the semiconductor effects are accounted in the simulation simply by virtue of a uniform conductivity or complex dielectric constant within the semiconductor material.

When an electromagnetic wave propagates along an MIS interconnect, the screening effect of charged carriers in the semiconductor prohibits the electromagnetic field from penetrating deep into the semiconductor, in addition to the attenuation effect arising from energy dissipation. In order to describe the behavior of semiconductor as solid-state plasma, the motion equations of charged carriers should be included in the simulation [18]. In other words, a formula combining the motion equations of carriers and Maxwell's equations is required in the device-level simulation in order to include the interaction mechanism between the electromagnetic field and charged carriers in semiconductor.

In [19], the propagation property of the fundamental mode in a biased parallel-plate MIS waveguide was investigated using a transport-based analysis. A formulation incorporating Maxwell's equations and the motion equations of carriers was first linearized and then solved using the finite-difference scheme. The approach in [19] enabled the investigation of

Manuscript received December 12, 2000.

G. Wang was with the Center for Integrated Systems, Stanford University, Stanford, CA 94305 USA. He is now with Intpax Inc., Cupertino, CA 95014 USA and also with Wuhan University, Wuhan, Hubei 430072, China.

R. W. Dutton is with the Center for Integrated Systems, Stanford University, Stanford, CA 94305 USA.

C. S. Rafferty was with Bell Laboratories, Lucent Technologies, Murray Hill, NJ 07974 USA. He is now with the Semiconductor Processing Research Department, Agere Systems, Murray Hill, NJ 07974 USA.

Publisher Item Identifier S 0018-9480(02)03020-X.

carrier accumulation and depletion under the influence of an external dc bias, as well as the screening effect of carriers. The approach in [19] is, however, applicable only to small-signal analysis due to its linearization of the equations.

In this paper, a device-level simulation based on Maxwell's equations and the motion equations of carriers is presented to study the propagation characteristics of MIS interconnects. The nonlinearity in the motion equations of carriers is preserved and included in the simulation. Thus, this approach is suitable for both small- and large-signal analyses. In order to provide a fast and robust simulation, advanced numerical algorithms such as finite-element discretization, sparse matrix scheme, matrix balancing, and multidimensional Newton's iterations have been utilized. Unlike the iterative algorithm in [19], where the equations are sequentially and separately solved at each iteration, this approach solves all the equations simultaneously, which reduces the number of iterations considerably. In addition, the boundary layer nature of the set of equations under study will be manifested theoretically and treated in a numerically consistent manner. This approach is able to provide detailed insight concerning field–carrier interactions, semiconductor substrate loss and nonlinearity, slow-wave effect, screening effects of carriers, and external bias effects.

II. Basic Formulation

In this section, the formula in the time domain for analyzing MIS interconnect structures is established and is then transformed into the frequency domain.

A. Time-Domain Formulation

In a homogeneous medium, Maxwell's equations are given by

$$\nabla \times \mathbf{E}(\mathbf{r},t) = -\mu \frac{\partial \mathbf{H}(\mathbf{r},t)}{\partial t} \tag{1a}$$

$$\nabla \times \mathbf{H}(\mathbf{r},t) = \varepsilon \frac{\partial \mathbf{E}(\mathbf{r},t)}{\partial t} + \mathbf{J}(\mathbf{r},t) \tag{1b}$$

$$\nabla \cdot \mathbf{E}(\mathbf{r},t) = \frac{\rho(\mathbf{r},t)}{\varepsilon} \tag{1c}$$

$$\nabla \cdot \mathbf{H}(\mathbf{r},t) = 0 \tag{1d}$$

where $\mathbf{E}$ and $\mathbf{H}$ are, respectively, the electric and magnetic fields, $\mathbf{J}$ is the conduction current density, ρ is the (net) electric charge density, and ε and μ are, respectively, the permittivity and permeability of the medium.

Equation (1d) can be viewed as a direct consequence of (1a), whereas (1b) and (1c) imply the current continuity

$$\nabla \cdot \mathbf{J}(\mathbf{r},t) + \frac{\partial \rho(\mathbf{r},t)}{\partial t} = 0. \tag{2}$$

Therefore, the set of independent equations from Maxwell's equations consists of (1a), (1b), and (2).

In dielectric materials, the electric charge density ρ is always zero. On the other hand, in a semiconductor medium, the electric charge density is given as

$$\rho(\mathbf{r},t) = q\big[p(\mathbf{r},t) - n(\mathbf{r},t) + N(\mathbf{r})\big] \tag{3}$$

where p and n are, respectively, the hole and electron densities, N is the net doping distribution that is, respectively, positive or negative for the relative excess of donors or acceptors, and q is the elementary charge.

In a semiconductor medium, the motion of carriers is governed by the following equations:

$$\tau_n \frac{\partial \mathbf{J}_n(\mathbf{r},t)}{\partial t} + \mathbf{J}_n(\mathbf{r},t) = q\mu_n n(\mathbf{r},t)\mathbf{E}(\mathbf{r},t) + qD_n \nabla n(\mathbf{r},t) \tag{4a}$$

$$\tau_p \frac{\partial \mathbf{J}_p(\mathbf{r},t)}{\partial t} + \mathbf{J}_p(\mathbf{r},t) = q\mu_p p(\mathbf{r},t)\mathbf{E}(\mathbf{r},t) - qD_p \nabla p(\mathbf{r},t) \tag{4b}$$

where $\mathbf{J}_n$ and $\mathbf{J}_p$ are, respectively, the electron and hole current densities, μ_n and μ_p are, respectively, effective carrier mobilities of electrons and holes, D_n and D_p are, respectively, diffusion coefficients for electrons and holes, and τ_n and τ_p are, respectively, average collision times of electrons and holes.

Note that the total conduction current density is the sum of the electron and hole current densities

$$\mathbf{J}(\mathbf{r},t) = \mathbf{J}_n(\mathbf{r},t) + \mathbf{J}_p(\mathbf{r},t). \tag{4c}$$

The current continuity (2) is usually written into two equations in terms of $\mathbf{J}_n$ and $\mathbf{J}_p$ as follows:

$$\frac{\partial n(\mathbf{r},t)}{\partial t} = \frac{1}{q}\nabla \cdot \mathbf{J}_n(\mathbf{r},t) - u(\mathbf{r},t) \tag{5a}$$

$$\frac{\partial p(\mathbf{r},t)}{\partial t} = -\frac{1}{q}\nabla \cdot \mathbf{J}_p(\mathbf{r},t) - u(\mathbf{r},t) \tag{5b}$$

where $u(\mathbf{r},t)$ is the total net recombination rate of electrons and holes.

In summary, the complete set of equations in the time domain consists of (1a), (1b), (4a), (4b), (5a) and (5b). This set of equations along with the properly devised boundary conditions can completely characterize the property of MIS structures.

B. Frequency-Domain Formulation

The nonlinear terms $n \cdot \mathbf{E}$ and $p \cdot \mathbf{E}$ in the time-domain formulation introduce signal distortion, which consists of various harmonics in the frequency domain. For a guided wave propagating along the z-direction, the fundamental component of an arbitrary variable $v(\mathbf{r},t)$ takes the form $v^{(1)}(x,y)e^{-\gamma z + j\omega t}$, where ω denotes the fundamental (angular) frequency and γ represents the propagation factor. Therefore, the product of two fundamental mode quantities $v_1^{(1)}(x,y)e^{-\gamma z + j\omega t}$ and $v_2^{(1)}(x,y)e^{-\gamma z + j\omega t}$ will result in a second harmonic quantity $v_1^{(1)}(x,y)v_2^{(1)}(x,y)e^{-2\gamma z + j2\omega t}$, and so on. In general, an $(m+n)$th harmonic quantity $v_1^{(m)}(x,y)v_2^{(n)}(x,y)e^{-(m+n)\gamma z + j(m+n)\omega t}$ can be generated from the product of an mth harmonic quantity $v_1^{(m)}(x,y)e^{-m\gamma z + jm\omega t}$ and an nth harmonic quantity $v_2^{(n)}(x,y)e^{-n\gamma z + jn\omega t}$.

The above procedure can be rigorously formulated by virtue of Fourier analysis. A guided nonlinear wave $v(\mathbf{r},t)$, propagating along the z-direction, takes the generalized form as follows:

$$v(\mathbf{r},t) = \tilde{v}\left(x, y, t - \frac{z}{v}\right) \tag{6a}$$

where v denotes the propagation velocity that is a function of the fundamental frequency. Moreover, $v(\mathbf{r},t)$ is a periodic function with respect to t and the period is equal to $2\pi/\omega$. Hence, (6a) can be mathematically expanded in terms of Fourier series as follows:

$$v(\mathbf{r},t) = v^{(0)}(x,y) + \sum_{m=1}^{\infty} v^{(m)}(x,y)\cdot e^{-m\gamma z}\cdot e^{jm\omega t} \quad (6b)$$

where $v^{(0)}(x,y)$ denotes the steady-state solution, i.e., the static component, $v^{(1)}(x,y)$ is the fundamental mode, and $v^{(m)}(x,y)(m>1)$ represents the mth harmonic component of the variable under consideration. In a linearized problem, all the higher order harmonics vanish and only the fundamental mode is considered. Thus, the nonlinear wave reduces to a monotonic wave. For a general nonlinear problem, however, all the higher order harmonics can be nonzero and should be included in the analysis.

The harmonics in the expansion (6b) should not be confused with the nonlinear wave itself at multiples of the fundamental frequency. The nonlinear wave could exist for the entire frequency range, whereas the harmonics occur only at multiples of the fundamental frequency. Moreover, the harmonics cannot exist without the presence of the fundamental mode as the excitation source, that is, the harmonics cannot stand alone by themselves. On the other hand, the nonlinear wave can exist in its own right. The propagation factor γ that characterizes the propagation property of the nonlinear wave is generally a nonlinear function of the frequency. Therefore, the propagation factor $\gamma(\varpi)|_{\varpi=m\omega}$ of the nonlinear wave at $\varpi = m\omega$ is usually unequal to $m\gamma(\omega)$ and irrelevant to the z dependence factor $e^{-m\gamma z}$ of the mth harmonic in the expansion (6b).

Substitution of the form (6b) into the time-domain formulation leads to

$$\nabla^2 E_z^{(m)}(x,y) + m^2(k^2+\gamma^2)E_z^{(m)}(x,y) = jm\omega\mu\left[J_{nz}^{(m)}(x,y) + J_{pz}^{(m)}(x,y)\right] - \frac{qm\gamma}{\varepsilon}\left[p^{(m)}(x,y) - n^{(m)}(x,y)\right] \quad (7a)$$

$$\nabla^2 \mathbf{E}_{xy}^{(m)}(x,y) + m^2(k^2+\gamma^2)\mathbf{E}_{xy}^{(m)}(x,y) = jm\omega\mu\left[\mathbf{J}_{nxy}^{(m)}(x,y) + \mathbf{J}_{pxy}^{(m)}(x,y)\right] + \frac{q}{\varepsilon}\nabla\left[p^{(m)}(x,y) - n^{(m)}(x,y)\right] \quad (7b)$$

$$jm\omega n^{(m)}(x,y) = \frac{1}{q}\nabla\cdot\mathbf{J}_{nxy}^{(m)}(x,y) - \frac{m\gamma}{q}J_{nz}^{(m)}(x,y) - u^{(m)}(x,y) \quad (8a)$$

$$jm\omega p^{(m)}(x,y) = -\frac{1}{q}\nabla\cdot\mathbf{J}_{pxy}^{(m)}(x,y) + \frac{m\gamma}{q}J_{pz}^{(m)}(x,y) - u^{(m)}(x,y) \quad (8b)$$

$$(1+jm\omega\tau_n)\mathbf{J}_n^{(m)}(x,y) = q\mu_n\sum_{s=0}^{m}\left[n^{(s)}(x,y)\mathbf{E}^{(m-s)}(x,y)\right] + qD_n\nabla n^{(m)}(x,y) - \hat{\mathbf{z}}qD_n m\gamma n^{(m)}(x,y) \quad (9a)$$

$$(1+jm\omega\tau_p)\mathbf{J}_p^{(m)}(x,y) = q\mu_p\sum_{s=0}^{m}\left[p^{(s)}(x,y)\mathbf{E}^{(m-s)}(x,y)\right] - qD_p\nabla p^{(m)}(x,y) + \hat{\mathbf{z}}qD_p m\gamma p^{(m)}(x,y) \quad (9b)$$

and

$$jm\omega\mathbf{H}^{(m)}(x,y) = -\frac{1}{\mu}\left[\nabla\times\mathbf{E}^{(m)}(x,y) + \hat{\mathbf{x}}m\gamma E_y^{(m)}(x,y) - \hat{\mathbf{y}}m\gamma E_x^{(m)}(x,y)\right] \quad (10)$$

where $k = \omega\sqrt{\mu\varepsilon}$ is the wavenumber in the medium, $\mathbf{J}_{xy}^{(m)}(x,y) = \hat{\mathbf{x}}J_x^{(m)}(x,y) + \hat{\mathbf{y}}J_y^{(m)}(x,y)$, and $\mathbf{E}_{xy}^{(m)}(x,y) = \hat{\mathbf{x}}E_x^{(m)}(x,y) + \hat{\mathbf{y}}E_y^{(m)}(x,y)$. During the derivation of (7a) and (7b), the magnetic field has been eliminated from (1a) and (1b), and the divergence equation is exploited as follows:

$$\nabla\cdot\mathbf{E}_{xy}^{(m)}(x,y) - m\gamma E_z^{(m)}(x,y) = \frac{q}{\varepsilon}\left[p^{(m)}(x,y) - n^{(m)}(x,y)\right]. \quad (11)$$

Theoretically, (7a) and (7b) are the equations needed for determining the electrical field components. However, numerical analysis of (7a) and (7b) may lead to spurious solutions [20], which do not satisfy the divergence condition (11). In a numerical analysis such as finite-element analysis, the basis functions for expanding the unknowns are merely required to be continuous, but not differentiable. Hence, a numerical solution satisfies the governing differential equations only in a weak sense. Due to the lack of sufficient differentiability, the implication of (11) by (7a) and (7b) no longer holds. As a consequence, a weak solution of (7a) and (7b) may not meet the divergence condition (11). To prevent spurious solutions, it is a common practice to incorporate the divergence condition (11) into the basic (7b) during the course of numerical analysis.

The complete formula in the frequency domain consists of (7a)–(10). Careful examination on these equations reveals that any given harmonic depends on the lower order harmonics only. Therefore, the harmonics can be recursively obtained from a lower order harmonic to a higher order harmonic, starting from the static solution. The solution to the static equations can be readily attained using the standard approach, in which a scalar potential ϕ is introduced through $\mathbf{E}^{(0)} = -\nabla\phi$ and solved along with the static carrier concentrations $n^{(0)}$ and $p^{(0)}$.

III. Analysis of MIS Waveguide Structures

The configuration of an MIS waveguide structure is shown in Fig. 1. In this section, the general frequency domain formula obtained in Section II is applied to MIS waveguide structures, and then boundary conditions are devised for the frequency-domain equations. Based on the frequency-domain formula, a finite-element analysis can be developed. Some special considerations to enhance the finite-element solution are addressed.

A. Basic Equations for MIS Waveguide Structures

A parallel-plate waveguide structure extends from $y=-\infty$ to $y=\infty$. Hence, all the physical quantities are uniformly dis-

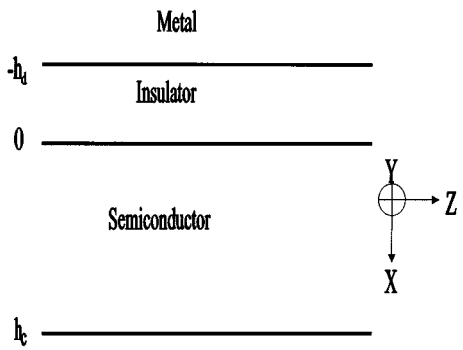

Fig. 1. Configuration of an MIS waveguide structure.

tributed along the y-direction, i.e., they are independent of the y coordinate. Moreover, the dominant mode in a parallel-plate waveguide is a TM mode. For TM modes, the magnetic field has only a y component and, thus, the electric field has no y component, as implied by (10). Hence, (7a)–(10) lead to

$$\frac{\partial^2 E_z^{(m)}(x)}{\partial x^2} + m^2\left(k_c^2+\gamma^2\right)E_z^{(m)}(x) = jm\omega\mu\left[J_{nz}^{(m)(r)}(x)+J_{pz}^{(m)(r)}(x)\right] - \frac{qm\gamma}{\varepsilon}\left[p^{(m)}(x)-n^{(m)}(x)\right] \tag{12a}$$

$$jm\omega n^{(m)}(x) = \frac{1}{q}\frac{\partial J_{nx}^{(m)}(x)}{\partial x} - \frac{m\gamma}{q}J_{nz}^{(m)}(x) - u^{(m)}(x) \tag{12b}$$

$$jm\omega p^{(m)}(x) = -\frac{1}{q}\frac{\partial J_{px}^{(m)}(x)}{\partial x} + \frac{m\gamma}{q}J_{pz}^{(m)}(x) - u^{(m)}(x) \tag{12c}$$

and

$$E_x^{(m)}(x) = -\frac{m\gamma}{m^2(k^2+\gamma^2)}\frac{\partial E_z^{(m)}(x)}{\partial x} + \frac{jm\omega\mu}{m^2(k^2+\gamma^2)}\left[J_{nx}^{(m)}(x)+J_{px}^{(m)}(x)\right] \tag{12d}$$

$$H_y^{(m)}(x) = \frac{1}{jm\omega\mu}\left[\frac{\partial E_z^{(m)}(x)}{\partial x} + m\gamma E_x^{(m)}(x)\right] \tag{12e}$$

where

$$(1+jm\omega\tau_n)\mathbf{J}_n^{(m)(0)}(x) = q\mu_n n^{(0)}(x)\mathbf{E}^{(m)}(x) \tag{13a}$$

$$(1+jm\omega\tau_p)\mathbf{J}_p^{(m)(0)}(x) = q\mu_p p^{(0)}(x)\mathbf{E}^{(m)}(x) \tag{13b}$$

$$(1+jm\omega\tau_n)\mathbf{J}_n^{(m)}(x) = q\mu_n\sum_{s=0}^{m}\left[n^{(s)}(x)\mathbf{E}^{(m-s)}(x)\right] + qD_n\nabla n^{(m)}(x) - \hat{\mathbf{z}}qD_n m\gamma n^{(m)}(x) \tag{13c}$$

$$(1+jm\omega\tau_p)\mathbf{J}_p^{(m)}(x) = q\mu_p\sum_{s=0}^{m}\left[p^{(s)}(x)\mathbf{E}^{(m-s)}(x)\right] - qD_p\nabla p^{(m)}(x) + \hat{\mathbf{z}}qD_p m\gamma p^{(m)}(x) \tag{13d}$$

$$\mathbf{J}_n^{(m)(r)}(x) = \mathbf{J}_n^{(m)}(x) - \mathbf{J}_n^{(m)(0)}(x)$$
$$\mathbf{J}_p^{(m)(r)}(x) = \mathbf{J}_p^{(m)}(x) - \mathbf{J}_p^{(m)(0)}(x) \tag{13e}$$

$$k_c^2 = k^2 - \frac{j\omega\mu\sigma^{(0)}(x)}{m}$$
$$\sigma^{(0)}(x) = q\left[\frac{\mu_n n^{(0)}(x)}{1+jm\omega\tau_n} + \frac{\mu_p p^{(0)}(x)}{1+jm\omega\tau_p}\right]. \tag{13f}$$

Equation (12d) is obtained by incorporating (11) into (7b), which is able to prevent spurious modes in the numerical solution.

B. Boundary Conditions

By accounting for the boundary condition $E_z^{(m)}(-h_d)=0$ on the metal surface, the field components in the dielectric layer can be obtained as follows:

$$E_z^{(m)}(x) = -\frac{A^{(m)}k_d}{\gamma}\sin\left[mk_d(x+h_d)\right] \tag{14a}$$

$$E_x^{(m)}(x) = A^{(m)}\cos\left[mk_d(x+h_d)\right] \tag{14b}$$

$$H_y^{(m)}(x) = \frac{j\omega\varepsilon_d A^{(m)}}{\gamma}\cos\left[mk_d(x+h_d)\right] \tag{14c}$$

where ε_d and μ_d are, respectively, the permittivity and permeability of the dielectric layer, and $k_d=\sqrt{\omega^2\mu_d\varepsilon_d+\gamma^2}$. Note that $A^{(1)}$ is an arbitrary constant depending on the excitation magnitude, while $A^{(m)}(m>1)$ is to be determined.

The boundary conditions on the interface between the insulator and semiconductor are as follows:

$$E_z^{(m)}(0^+) = E_z^{(m)}(0^-) = -\frac{A^{(m)}k_d}{\gamma}\sin(mk_d h_d) \tag{15a}$$

$$H_y^{(m)}(0^+) = H_y^{(m)}(0^-) = \frac{j\omega\varepsilon_d A^{(m)}}{\gamma}\cos(mk_d h_d) \tag{15b}$$

$$J_{nx}^{(m)}(0) = J_{px}^{(m)}(0) = 0. \tag{15c}$$

The ground plane at $x=h_c$ is usually far away from the signal line, i.e., the value of h_c is generally much larger than the Debye length. Hence, the ground plane may have little impact on the propagation characteristics. The boundary conditions on the ground plane are prescribed as

$$E_z^{(m)}(h_c) = 0 \tag{15d}$$

$$n^{(m)}(h_c) = p^{(m)}(h_c) = 0. \tag{15e}$$

For the fundamental mode, eliminating the arbitrary constant $A^{(1)}$ in (15a) and (15b) leads to

$$\frac{E_z^{(1)}(0^+)}{H_y^{(1)}(0^+)} = -\frac{k_d}{j\omega\varepsilon_d}\tan(k_d h_d). \tag{16}$$

Equation (16) provides a nonlinear algebraic equation for determining the propagation factor γ. Given an excitation magnitude $A^{(1)}$, (12a)–(12e) and (16) along with boundary conditions (15a) and (15c)–(15e) completely determine the field components, carrier concentrations, and propagation factor for the fundamental mode. Note that the boundary condition (15b) is automatically fulfilled provided that (15a) and (16) are imposed.

For a high-order harmonic with $m > 1$, (12e) and (15b) are compatible only if one of the following conditions holds:

$$\frac{E_z^{(m)}(0^+)}{H_y^{(m)}(0^+)} = -\frac{mk_d}{jm\omega\varepsilon_d}\tan(mk_dh_d) \tag{17}$$

or

$$A^{(m)} = 0 \tag{18}$$

where the mth harmonic components $E_z^{(m)}$ and $H_y^{(m)}$ are assumed to be the solution of (12a)–(12e) under the boundary conditions (15a) and (15c)–(15e).

In general, the propagation factor γ determined from (16) hardly meets the condition given by (17). Therefore, (18) must be imposed as the compatibility condition. This implies that the high-order harmonics due to the semiconductor nonlinearity are confined in the semiconductor and do not penetrate into the insulator.

If (17) happens to be satisfied, the solution would not be unique since any arbitrary $A^{(m)}$ could result in a solution, which is a phenomenal characteristic of shock waves or resonance. The reason for the resonance occurrence is because under (17), the mth harmonic is satisfying the identical set of equations as the fundamental mode at frequency $f^{(m)} = mf$. Physically, the local mth harmonic contributions due to the semiconductor nonlinearity are able to propagate as fundamental mode waves along the waveguide and, thus, be summed in phase along their propagation paths to give rise to resonance.

Under the compatibility condition (18), (12a)–(12e) along with the boundary conditions (15a) and (15c)–(15e) completely determine the mth harmonic field components and carrier concentrations (where $m > 1$).

C. Some Considerations on Finite-Element Analysis

The frequency-domain formula developed in Section III-A and B can be discretized using the standard finite-element procedure [21]. Since all the equations under consideration have derivatives up to the second order, the weak form of the finite-element analysis contains derivatives up to the first order. Hence, the interpolation (shape) functions with C^0 continuity are sufficient for the problem under study.

After substitution of $J_{nx}^{(m)}$ and $J_{px}^{(m)}$, (12b) and (12c) contain the second-order derivatives $\partial^2 n^{(m)}/\partial x^2$ and $\partial^2 p^{(m)}/\partial x^2$, respectively. In (12b), the ratio between the coefficients of $\partial^2 n^{(m)}/\partial x^2$ and $n^{(m)}$ is roughly of the order of L_{Dn}^2, where $L_{Dn} = \sqrt{\varepsilon D_n/qn^{(0)}\mu_n}$ is the n-type Debye length. Similarly, in (12c), the ratio between the coefficients of $\partial^2 p^{(m)}/\partial x^2$ and $p^{(m)}$ is roughly of the order of L_{Dp}^2, where $L_{Dp} = \sqrt{\varepsilon D_p/qp^{(0)}\mu_p}$ is the p-type Debye length.

Note that the Debye length is generally much smaller than the dimension of the structure under consideration. Mathematically, either (12b) or (12c) results in a boundary layer problem [22], which implies a solution with a fast varying factor $e^{-x/L_{Dn}}$ or $e^{-x/L_{Dp}}$ within a very thin layer of the order of the Debye length. Physically, an accumulation-depletion layer of carriers appears in the semiconductor near the interface at $x = 0$. In order for modeling the fast decay behavior of carrier concentrations in the accumulation-depletion layer, an adaptive meshing scheme is employed to allocate finer elements at locations closer to the interface $x = 0$ in the finite-element discretization.

Theoretically, the x component of electrical field should automatically fulfill the boundary condition

$$E_x^{(m)}(0^+) = \frac{\varepsilon_d}{\varepsilon}E_x^{(m)}(0^-) = \frac{\varepsilon_d}{\varepsilon}A^{(m)}\cos(mk_dh_d). \tag{19}$$

However, the weak solution may not satisfy (19) due to the weak sense of the numerical solution and the error introduced by numerical evaluation of the derivative term in (12d). The consequences become severe because the solution in the accumulation-depletion layer is quite sensitive. In order to remove the degradation of accuracy near the interface at $x = 0$ and enhance the overall solution convergence, a boundary term imposing (19) at $x = 0$ has been added into the weak form regarding to (12d). By so doing, the numerical solution is actually required to satisfy (19) at $x = 0$ while meeting (12d) everywhere else.

Since the equations are nonlinear in γ, it is essentially a nonlinear system of equations for the fundamental mode. Newton's method [23] can be used to solve such a nonlinear system of equations. Unlike the iterative algorithm in [19], which solves the equations sequentially and separately at each iteration, all the equations are simultaneously solved using multidimensional Newton's method in this scheme, which reduces the number of iterations considerably.

For high-order harmonics, the equations turn out to be linear and, thus, can be solved by the standard matrix technique [24]. To gain fast computational speed and save memory, sparse matrix schemes have been utilized for solving linear equations. To circumvent the large disparity of the magnitude among unknown variables, matrix balancing is also adapted. Further detailed discussions on numerical aspects of this scheme including multidimensional Newton's method, finite-element discretization, and matrix manipulation can be found in [26].

IV. Numerical Results

In this section, numerical results are presented to validate the computer program and demonstrate capabilities of this device-level frequency-domain (DLFD) scheme. For all the numerical examples, unless otherwise mentioned, the following geometrical and material parameters were assumed: $\varepsilon = 11.9\varepsilon_0$, $\varepsilon_d = 3.9\varepsilon_0$, $\mu = \mu_d = \mu_0$, $\mu_n = 1500\,\text{cm}^2/(\text{v}\cdot\text{s})$, $\mu_p = 450\,\text{cm}^2/(\text{v}\cdot\text{s})$, $D_n = \mu_n\kappa T/q$, $D_p = \mu_p\kappa T/q$, $T = 300\,\text{K}$, $\tau_n = 2.2156\times 10^{-13}$ s, $\tau_p = 5.2706\times 10^{-14}$ s, $h_d = 0.05$ μm, and $h_c = 100$ μm, where ε_0 and μ_0 are, respectively, the permittivity and permeability in vacuum, and κ is the Boltzmann constant. The semiconductor was assumed to be n-type silicon with donor impurity concentration $N_d = 10^{17}\,\text{cm}^{-3}$. The metal work function was chosen in such a way that a flat-band condition would be attained in the absence of external bias. Under the assumption of small disturbance from equilibrium, the net recombination rates can be approximately expressed as $u^{(m)} = p^{(m)}/t_p$ by virtue of the Shockley–Read–Hall recombination model. The hole lifetime t_p was taken to be 2.5×10^{-3} s in the calculation. Various excitations with $A^{(1)}$ ranging from 10^{-2} v/cm to 10^5 v/cm have been applied in the simulation.

In order to tackle the boundary layer nature, the mesh grid takes a much smaller size at a location closer to the interface

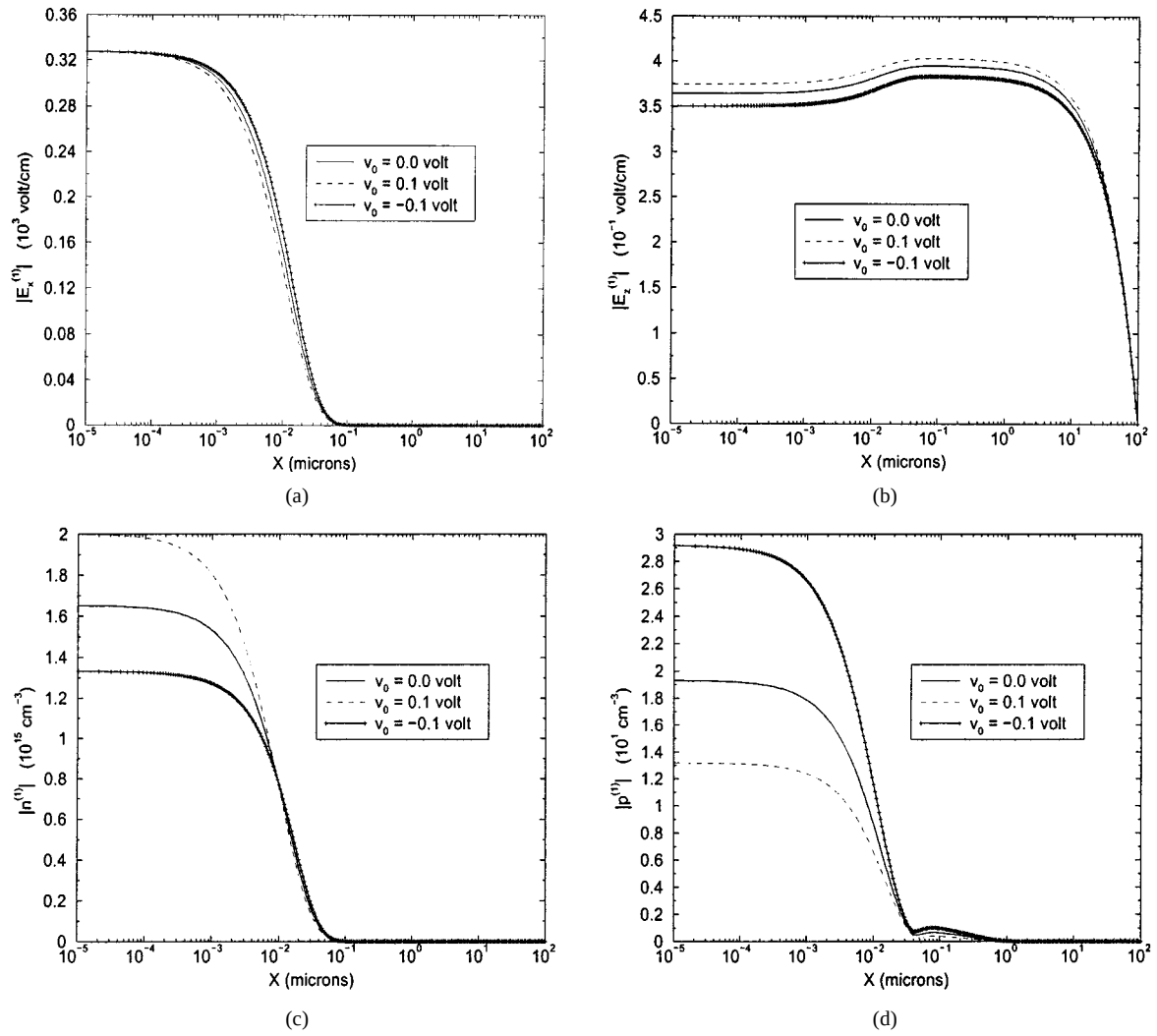

Fig. 2. Magnitude of the fundamental mode in the semiconductor. (a) Electric-field component $E_x^{(1)}$. (b) Electric-field component $E_z^{(1)}$. (c) Electron concentration $n^{(1)}$. (d) Hole concentration $p^{(1)}$.

at $x = 0$. In specific, for the numerical example below, the mesh size starts as small as 10^{-5} μm at $x = 0$, and gradually increases to 5 μm at $x = 100$ μm. By so doing, the mesh grid is fine enough to capture the boundary layer behavior in the accumulation-depletion layer, whereas keeps the entire problem manageable by easily accessible computing resources such as personal computers. The utilization of sparse matrix techniques results in an algorithm of complexity $O(N^2)$, where N denotes the total number of unknowns.

Figs. 2 and 3 illustrate the magnitude distributions of field components and carrier concentrations for the fundamental mode, the second-order harmonic, and the third-order harmonic along the vertical direction at a fundamental frequency $f = 5$ GHz, when an excitation with $A^{(1)} = 10^3$ v/cm was applied. The cases with three different external bias conditions, i.e., negative bias -0.1 v, no bias, and positive bias $+0.1$ v, were examined. For these respective external bias conditions, the propagation factor γ was obtained as $0.0024549 + j0.0065734$, $0.0026608 + j0.0067883$, and $0.002938 + j0.0068985$. The real part of propagation factor gives the attenuation constant α, whereas its imaginary part corresponds to the phase constant β. The above values of propagation factor result in the normalized phase constant $\beta/k_0 = 62.7279, 64.7787$, and 65.8303 and the attenuation constant $21.323, 23.114$, and 25.5191 dB/mm, respectively, where k_0 denotes the wavenumber in vacuum. The large ratio between the phase constant and vacuum wavenumber indicates that the MIS waveguide structure exhibits a slow-wave phenomenon. Moreover, the attenuation constant provides a direct account for the semiconductor substrate loss.

Some phenomena reported in the small-signal analysis of [19] can be observed in the solution of the fundamental mode, as shown in Fig. 2. In most previous work on studying MIS structures (e.g., see [6]–[17]), semiconductor substrates were described by a uniform conductivity model in which the semiconductor is treated as a uniform lossy material and the electrical property of the semiconductor is characterized by its conductivity and dielectric constant. Using such a uniform conductivity model [3], [25], the propagation factor can be readily obtained as a complex value $0.0027554 + j0.00686443$, which provides a close approximation to the actual result attained using the device-level simulation. Nevertheless, the device-level simulation is able to offer detailed insight regarding field–carrier interaction mechanisms, as well as external bias effects, whereas the uniform conductivity model fails to do so. The device-level sim-

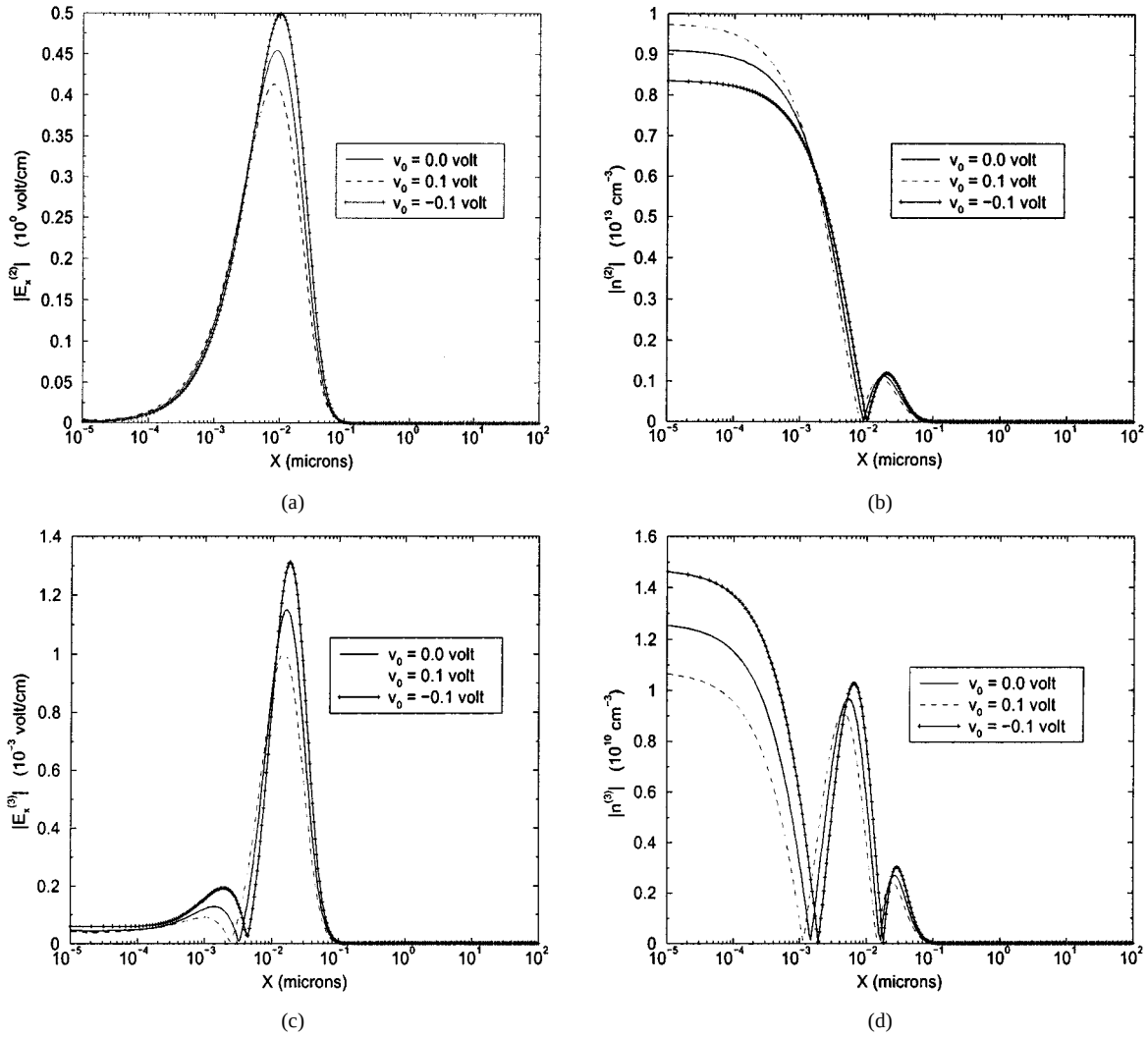

Fig. 3. Magnitude of high-order harmonics in the semiconductor. (a) Electric-field component $E_x^{(2)}$ of the second harmonic. (b) Electron concentration $n^{(2)}$ of the second harmonic. (c) Electric-field component $E_x^{(3)}$ of the third harmonic. (d) Electron concentration $n^{(3)}$ of the third harmonic.

ulation shows a strong coupling effect between the transverse component $E_x^{(1)}$ of electrical field and charged carriers, which leads to a completely different solution in the accumulation-depletion layer from that predicted by the uniform conductivity model. As indicated in the plots, the screening effect of the carriers near the accumulation-depletion layer prevents the electrical field from penetrating the semiconductor to beyond a few Debye lengths.

Furthermore, this device-level simulation is capable of investigating the nonlinearity effect and predicting harmonics quantitatively, as shown in Fig. 3. It is of interest to note that some sidelobes appear in the amplitude plots of majority carrier concentrations for high-order harmonics. The second harmonic is generated by field–carrier interactions among the fundamental mode, whereas the third harmonic is due to field–carrier interactions between the fundamental mode and second harmonic. Therefore, intuitively, the second harmonic is expected to act in more complex way than the fundamental mode. Moreover, the third harmonic might exhibit even wilder behavior than the second harmonic. The intuition agrees well with the simulation results, as shown by Fig. 3, where more sidelobes are observed for a higher order harmonic. Moreover, the location where the electric field $E_x^{(2)}$ reaches its maximum coincides with the zero-crossing point of the majority carrier concentration $n^{(2)}$. A similar phenomenon to the third harmonic can be also observed between the electric field $E_x^{(3)}$ and the majority carrier concentration $n^{(3)}$. The zero-crossing points correspond to the regions where the majority carrier concentrations undertake rapid changes, which could induce strong electric fields locally.

The simulations were also performed for several other excitations with $A^{(1)}$ ranging from 10^{-2} v/cm to 10^5 v/cm. For each of these excitations, plots identical to Figs. 2 and 3 can be obtained, except that appropriate scaling factors need to be used. In Figs. 2 and 3, the scaling factors are shown in the brackets along with the units at the vertical axis labels, i.e., the scaling factors are 10^3, 10^{-1}, 10^{15}, 10, 10^0, 10^{13}, 10^{-3}, and 10^{10} for unknowns $E_x^{(1)}$, $E_z^{(1)}$, $n^{(1)}$, $p^{(1)}$, $E_x^{(2)}$, $n^{(2)}$, $E_x^{(3)}$, and $n^{(3)}$, respectively. These scaling factors are an excellent measure for the order of magnitude of unknowns. Fig. 4 depicts the scaling factors versus the excitation magnitude $A^{(1)}$ for the interested unknown variables.

It can be both theoretically proven and numerically observed that the fundamental mode is linearly proportional to the excitation magnitude $A^{(1)}$. Using the fact, the fundamental mode for

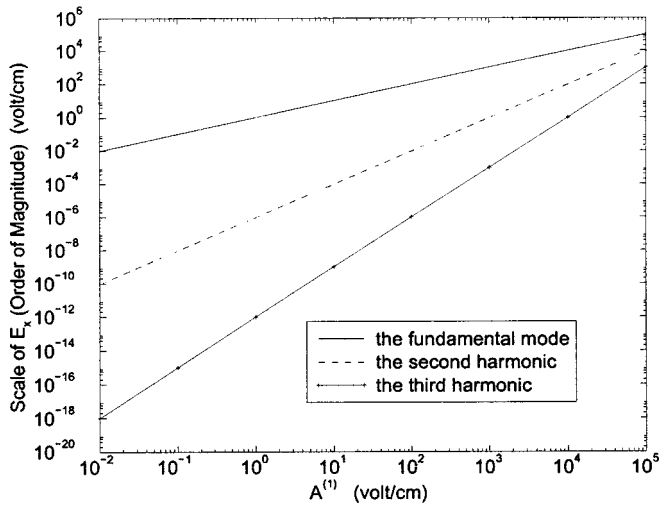

(a)

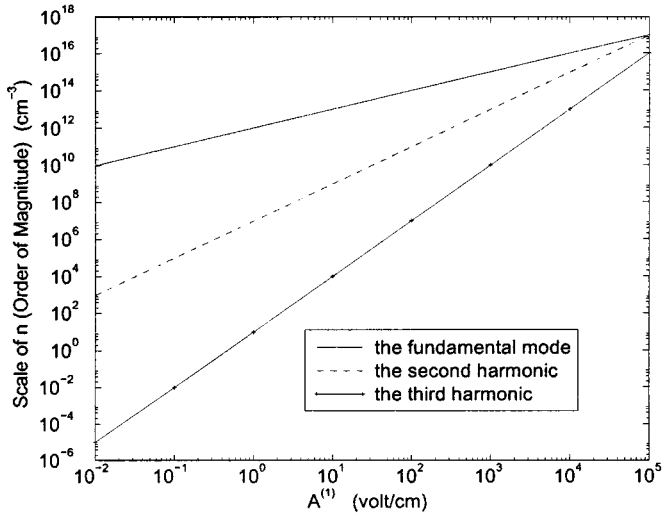

(b)

Fig. 4. Scaling factors (orders of magnitudes) of the fundamental mode, second harmonic, and third harmonic. (a) x components of electric field. (b) Electron concentrations.

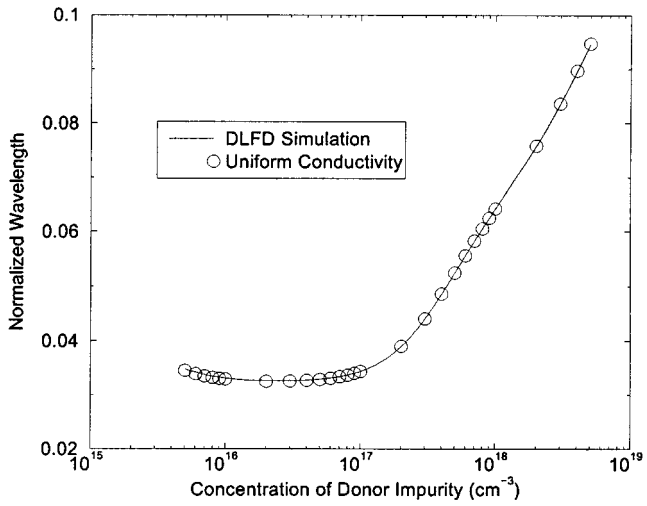

(a)

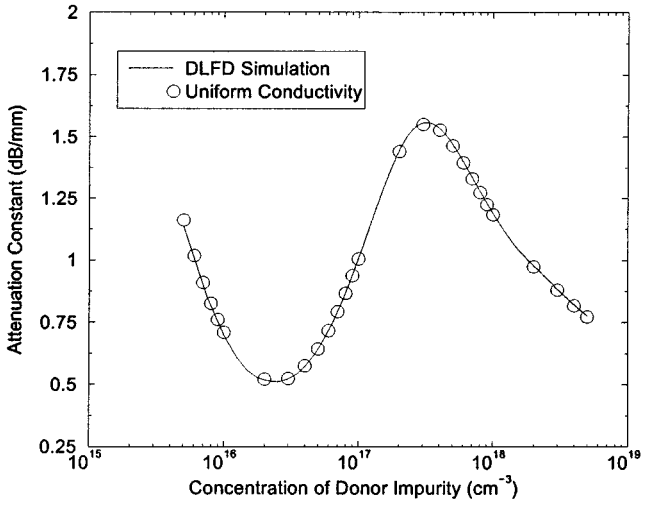

(b)

Fig. 5. Propagation characteristics versus the impurity concentration. (a) Normalized wavelength. (b) Attenuation constant.

the excitation with $A^{(1)} = 10^{-2}$ v/cm can be readily obtained by scaling plots in Fig. 2 with a factor 10^{-5}, which gives results in a close agreement with those from the small-signal analysis, i.e., [19, Figs. 6–9]. Some slight discrepancies exhibited by the minority carrier concentration $p^{(1)}$ might be caused by a different recombination formula used in the calculation from that in [19]. Two distinct net recombination rates were employed in [19] for electrons and holes, respectively, which might lead to a violation of the basic charge conservation principle. In this study, a single net recombination rate formula is applied to account for contributions from both electrons and holes, which eliminates this violation. The propagation factor γ is usually a function of geometrical and material parameters and external bias, but independent of the excitation strength. Hence, the propagation factors are the same for all the excitations.

Moreover, Fig. 4 reveals that the second and third harmonics are, respectively, proportional to $[A^{(1)}]^2$ and $[A^{(1)}]^3$. In general, it can be expected that the mth harmonic is proportional to $[A^{(1)}]^m$. When the excitation becomes larger, the magnitudes of high-order harmonics get closer and more comparable to the magnitude of the fundamental mode and, thus, the nonlinearity becomes more severe. As shown in Fig. 4, the ratio between the magnitudes of a high-order harmonic and the fundamental mode is becoming unity when $A^{(1)}$ is approaching 10^6 v/cm and equivalently the maximum magnitude of $E_x^{(1)}$ is approaching 3.27×10^5 v/cm. Note that the breakdown field strength for silicon is about 3×10^5 v/cm. Therefore, a nearly unitary ratio between the magnitudes of the high-order harmonics and the fundamental mode is a clear indication of semiconductor breakdown. Mathematically, it implies that the solution can no longer be expressed by a series of harmonics because the series (6b) divergences and, thus, is invalid.

For an excitation with $A^{(1)} = 10^3$ v/cm, the high-order harmonics are very small fractions of the fundamental mode in magnitude, which are about or below 0.1% of the fundamental model. In this case, the MIS waveguide structure can be approximated as a linear-circuit element. However, for an excitation with $A^{(1)} = 10^5$ v/cm, the second harmonic is now about one-tenth of the fundamental mode in magnitude, which can no

longer be neglected. In the later case, the MIS waveguide structure should be treated as a nonlinear circuit element. Given that the insulator thickness is 0.05 μm, the equivalent ac voltage to $A^{(1)} = 10^5$ v/cm is roughly 0.5 V. Roughly speaking, most of the voltage drop is applied across the insulator layer and, thus, the magnitude of electric field is linearly proportional to the insulator thickness for a given voltage. A thicker insulator layer is able to reduce the electric field in the semiconductor substrate and, thus, suffers less severe nonlinearity. For instance, if the insulator thickness is increased to be 0.5 μm, the second harmonic is then only approximately 1% of the fundamental mode in magnitude, although the ac voltage is still 0.5 V.

The signal propagation along an MIS interconnect depends strongly on the conductivity of the semiconductor substrate. Depending on its doping rate, the substrate conductivity can vary over a wide range, e.g., more than four decades from 1 S/m to 10^5 S/m when silicon is used as the substrate material. Fig. 5 depicts the phase and attenuation constants versus the impurity concentration for an MIS interconnect. In this calculation, the geometrical parameters are given as $h_d = 1$ μm and $h_c = 250$ μm, whereas all the physical parameters are assumed to be the same as those used in previous examples, except for the donor impurity concentration that varies over a range from $N_d = 5\times10^{15}$ cm^{-3} to $N_d = 5\times10^{18}$ cm^{-3}. The operating frequency is assumed to be 1 GHz, and no external bias is applied to this MIS structure. The results obtained using the uniform conductivity model [3], [25] are also shown in the plots for a purpose of comparison. As was expected, under zero bias, these two sets of solutions are in a close agreement. It is of interest to note that the attenuation oscillates as the substrate conductivity monotonically increases. When the substrate conductivity gets sufficient large, the slow-wave effect diminishes, which indicates that the skin effect becomes dominant for a good conducting substrate.

V. Conclusion

A device-level simulation has been presented for studying wave propagation along MIS interconnects. This simulation is based on a set of nonlinear equations consisting of the motion equations of charged carriers and Maxwell's equations for electromagnetic fields. The set of nonlinear equations is then transformed into the frequency domain and solved for a solution in terms of a fundamental mode and high-order harmonics. Finite-element analysis and the Newton's method are employed to discretize and solve the frequency-domain equations numerically. This device-level simulation provides quantitative predictions to propagation and attenuation constants, as well as detailed field and carrier distributions of the fundamental mode and high-order harmonics. This proposed device-level simulation scheme allows for large-signal analysis to be performed and is capable of studying detailed field–carrier interaction mechanisms, semiconductor substrate loss and nonlinearity, slow-wave effect, and external bias effect. It has been shown that the high-order harmonics due to the semiconductor nonlinearity are confined in the semiconductor and do not penetrate into the insulator in MIS waveguide structures.

References

[1] T. M. Hyltin, "Microstrip transmission on semiconductor dielectrics," *IEEE Trans. Microwave Theory Tech.*, vol. MTT-13, pp. 777–781, Nov. 1965.

[2] H. Guckel, P. A. Brennan, and I. Palocz, "A parallel-plate wave-guide approach to micro-miniaturized planar transmission lines for integrated circuits," *IEEE Trans. Microwave Theory Tech.*, vol. MTT-15, pp. 468–476, Aug. 1967.

[3] H. Hasegawa, M. Furukawa, and H. Yanai, "Properties of microstrip line on Si-SiO_2 system," *IEEE Trans. Microwave Theory Tech.*, vol. MTT-19, pp. 869–881, Nov. 1971.

[4] J. M. Jaffe, "A high-frequency variable delay line," *IEEE Trans. Electron Devices*, vol. ED-19, pp. 1292–1294, Dec. 1972.

[5] G. W. Hughes and R. M. White, "Microwave properties of nonlinear MIS and Schottky-barrier microstrip," *IEEE Trans. Electron Devices*, vol. ED-22, pp. 945–956, Oct. 1975.

[6] C. Seguinot, P. Kennis, P. Pribetich, and J. F. Legier, "Analytical model of the Schottky contact coplanar line," in *Proc. 14th Eur. Microwave Conf.*, Sept. 1984, pp. 160–165.

[7] J. K. Wee, Y. J. Park, H. S. Min, D. H. Cho, M. H. Seung, and H. S. Park, "Modeling the substrate effect in interconnect line characteristics of high-speed VLSI circuits," *IEEE Trans. Microwave Theory Tech.*, vol. 46, pp. 1436–1443, Oct. 1998.

[8] Y. Fukuoka, Y. Shih, and T. Itoh, "Analysis of slow-wave coplanar waveguide for monolithic integrated circuits," *IEEE Trans. Microwave Theory Tech.*, vol. MTT-31, pp. 567–573, July 1983.

[9] R. Sorrentino, G. Leuzzi, and A. Silbermann, "Characteristics of metal–insulator–semiconductor coplanar waveguide for monolithic microwave circuits," *IEEE Trans. Microwave Theory Tech.*, vol. MTT-32, pp. 410–416, Oct. 1984.

[10] T. G. Livernois and P. B. Katehi, "A generalized method for deriving the space-domain Green's function in a shielded, multilayer substrate structure with applications to MIS transmission lines," *IEEE Trans. Microwave Theory Tech.*, vol. 37, pp. 1761–1767, Nov. 1989.

[11] J. P. K. Gilb and C. A. Balanis, "MIS slow-wave structures over a wide range of parameters," *IEEE Trans. Microwave Theory Tech.*, vol. 40, pp. 2148–2154, Dec. 1992.

[12] J. C. Liou and K. M. Lau, "Analysis of slow-wave transmission lines on multi-layered semiconductor structures including conductor loss," *IEEE Trans. Microwave Theory Tech.*, vol. 41, pp. 814–829, May 1993.

[13] K. Wu and R. Vahldieck, "Hybrid-mode analysis of homogeneously and inhomogeneously doped low-loss slow-wave coplanar transmission lines," *IEEE Trans. Microwave Theory Tech.*, vol. 39, pp. 1348–1360, Aug. 1991.

[14] S. Chen, R. Vahldieck, and J. Huang, "Rigorous analysis of mode propagation and field scattering in silicon-based coplanar MIS slow wave structures with abrupt transitions to transmission lines on normal substrate," *IEEE Trans. Microwave Theory Tech.*, vol. 44, pp. 2487–2494, May 1996.

[15] T. Shibata and E. Sano, "Characterization of MIS structure coplanar transmission lines for investigation of signal propagation in integrated circuits," *IEEE Trans. Microwave Theory Tech.*, vol. 38, pp. 881–890, July 1990.

[16] M. Aubourg, J. Villotte, F. Godon, and Y. Garault, "Finite element analysis of lossy waveguide—Applications to microstrip lines on semiconductor substrate," *IEEE Trans. Microwave Theory Tech.*, vol. MTT-31, pp. 326–330, Apr. 1983.

[17] C. Tzuang and T. Itoh, "Finite element analysis of slow-wave Schottky contact printed lines," *IEEE Trans. Microwave Theory Tech.*, vol. MTT-34, pp. 1483–1489, Dec. 1986.

[18] C. M. Krowne and G. B. Tait, "Propagation in layered biased semiconductor structures based on transport analysis," *IEEE Trans. Microwave Theory Tech.*, vol. 37, pp. 711–722, Apr. 1989.

[19] K. Han and T. T. Y. Wong, "Space-charge wave considerations in MIS waveguide analysis," *IEEE Trans. Microwave Theory Tech.*, vol. 39, pp. 1126–1132, July 1991.

[20] K. D. Paulsen and D. R. Lynch, "Elimination of vector parasites in finite element Maxwell solutions," *IEEE Trans. Microwave Theory Tech.*, vol. 39, pp. 395–404, Mar. 1991.

[21] T. J. R. Hughes, *The Finite Element Method: Linear Static and Dynamic Finite Element Analysis*. Englewood Cliffs, NJ: Prentice-Hall, 1987.

[22] C. Bender and S. Orszag, *Advanced Mathematical Methods for Engineers*. New York: McGraw-Hill, 1978.

[23] J. E. Dennis and R. B. Schnabel, *Numerical Methods for Unconstrained Optimization and Nonlinear Equations*. Englewood Cliffs, NJ: Prentice-Hall, 1983.

[24] G. H. Golub and C. F. Van Loan, *Matrix Computations*, 3rd ed. Baltimore, MD: Johns Hopkins Univ. Press, 1996.
[25] D. F. Williams, "Metal–insulator–semiconductor transmission lines," *IEEE Trans. Microwave Theory Tech.*, vol. 47, pp. 176–181, Feb. 1999.
[26] G. Wang, "Coupled electromagnetic and device level investigations of metal–insulator–semiconductor interconnects," Ph.D. dissertation, Dept. Sci. Comput., Stanford Univ., Stanford, CA, 2001.

Gaofeng Wang (S'93–M'95–SM'01) was born in Hubei, China, on December 24, 1965. He received the Ph.D. degree in electrical engineering from the University of Wisconsin, Milwaukee, WI, in 1993, and the Ph.D. degree in scientific computing from Stanford University, Stanford, CA, in 2001.

From 1988 to 1990, he was with the Department of Space Physics, Wuhan University, Wuhan, China, where he was involved in research and teaching of radio-wave propagation in ionosphere and numerical methods for electromagnetic waves and fields. From 1990 to 1993, he was a Research Assistant with the Department of Electrical Engineering, University of Wisconsin. From 1993 to 1996, he was a Scientist with Tanner Research Inc., Pasadena, CA. From 1996 to 2001, he was a Principal Engineer with Synopsys Inc., Mountain View, CA. Since 2000, he has been a Chief Scientist with Intpax Inc., Cupertino, CA. He is also with Wuhan University. In the summer of 1999, he was a consultant with Bell Laboratories, Lucent Technologies, Murray Hill, NJ. Since 1998, he has been with Stanford University, Stanford, CA, as a member of the Technology Computer-Aided Design (CAD) Group. His research and development interests include electromagnetic theory, microwave engineering, computational electromagnetics, electronic design automation (EDA) software, signal integrity analysis, device modeling, wavelet applications in numerical analysis and image processing, and optical engineering. He has authored or co-authored over 50 technical papers, including 25 papers in leading archival scientific journals.

Robert W. Dutton (S'67–M'70–SM'80–F'84) received the B.S., M.S., and Ph.D. degrees from the University of California at Berkeley, in 1966, 1967, and 1970, respectively.

He is currently a Professor of electrical engineering with Stanford University, Stanford, CA, and Director of Research of the Center for Integrated Systems, Stanford University. He has held summer staff positions at Fairchild, Bell Telephone Laboratories, Hewlett-Packard, IBM Research, and Matsushita during 1967, 1973, 1975, 1977, and 1988 respectively. He has authored or co-authored over 2000 journal papers. He has graduated over four dozen doctorate students. His research interests focus on integrated circuit process, device, and circuit technologies—especially the use of computer-aided design (CAD) in device scaling and for RF applications.

Dr. Dutton was the editor-in-chief of the IEEE TRANSACTIONS ON COMPUTER-AIDED DESIGN OF INTEGRATED CIRCUITS AND SYSTEMS (1984–1986). He was the recipient of the 1987 IEEE J. J. Ebers and 1996 Jack Morton Awards and the 1988 Guggenheim Fellowship to study in Japan. He was elected to the National Academy of Engineering in 1991. He was also the recipient of the 1996 Jack A. Morton Award and the 2000 C&C Prize (Japan).

Conor S. Rafferty (S'85–M'87–SM'99–F'00) received the B.Sc. degree in physics, B.A. degree in mathematics, and M.Sc. degree in electrical engineering from Trinity College, Dublin, Ireland, and the Ph.D. degree in electrical engineering from Stanford University, Stanford, CA.

He currently heads the Semiconductor Processing Research Department, Agere Systems, Murray Hill, NJ, where he is the primary author of the third-generation process and device simulator PROPHET. His research is in the area of process simulation, silicon oxidation, ion implantation, and dopant diffusion for advanced microelectronics technologies. He co-authored the device simulator PISCES and process simulator SUPREM-4.